High Spatial Resolution BRDFs with Metallic powders Using Wave Optics Analysis

Anat Levin[1] Daniel Glasner[1] Ying Xiong[2] Frédo Durand[3] William Freeman[3] Wojciech Matusik[3] Todd Zickler[2]
[1]Weizmann Institute [2]Harvard [3]MIT CSAIL

Abstract

This manuscript completes the analysis of our SIGGRAPH 2013 paper [Levin et al. 2013], "Fabricating BRDFs at High Spatial Resolution Using Wave Optics" in which photolithography fabrication was used for manipulating reflectance effects. While photolithography allows for precise reflectance control, it is costly to fabricate. Here we explore an inexpensive alternative to micro-fabrication, in the form of metallic powders. Such powders are readily available at a variety of particle sizes and morphologies. Using an analysis similar to the micro-fabrication paper, we provide guidelines for the relation between the particles' shape and size and the reflectance functions they can produce.

Keywords: Fabrication, metallic powders, BRDF design, wave optics.

1 Powder-Based Reflectance

Photolithography allows precise control over micro-scale shape, but it is relatively costly for low production numbers, and it restricts fabrication to planar substrates. Thus, in order to complement the preceding analysis, we follow Johnson et al. [2011] and investigate the use of metallic powders for controlling appearance. These provide much cruder manipulation of reflectance, but they are a flexible and inexpensive alternative to photolithography. Metallic particles are available at a variety of morphologies and sizes, and they are relatively inexpensive. Typical prices are a few dollars per gram, with a single gram sufficient to cover a relatively large surface area.

It is quite challenging to model the exact arrangement in which particles lie when deposited onto substrate, because it depends on the method of application, the substrate properties, and various electrostatic forces. This section presents a model that expresses the surface as an assembly of independent copies of any basic shape, while ignoring occlusions and masking between nearby particles. While this model is very simple, we find that it is able to explain some of the observed phenomena.

Planar flakes: When a metallic powder consists of particles that are flat and wide flakes, these flakes will often be arranged into piecewise linear microstructures that can be approximated using the piecewise-flat model of Sect. 3. Thus, according to Claim 1 of [Levin et al. 2013] these powders produce glossy reflectance with the angular extent of the glossy lobe determined by the width of the flakes. An example of a flake-based powder is depicted in (Fig. 1(b-c)). These flakes are planar particles whose thickness is about $100-200nm$ and whose area is a few microns wide. A variety of sizes are commercially available. By selecting flake widths, we can approximately control the reflectance as described in [Levin et al. 2013]. An advantage of this flake-based approach is that since the number of depth values is not limited to a finite set, we can almost always achieve a pure glossy reflectance that does not contain any specular spike.

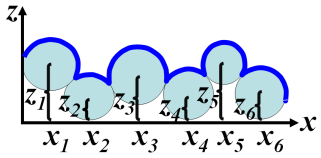

Figure 2: *The parameterization of a spheres surface.*

General particle morphologies: In a powder-based approach we are not restricted to flake-shaped particles. Many morphologies are available, including the spherical particles used by Johnson et. al [2011] for photometric stereo depth sensing. A SEM view of such a spherical powder is shown in Fig. 1(a).

We model the surface as being composed of copies of a basic shape $\vartheta(x)$. Until this point we dealt with piecewise flat surfaces, corresponding to a constant ϑ. However, $\vartheta(x)$ can encode other shapes, for example spheres. We denote by ϑ_{x_j,a_j} a copy of ϑ centered at x_j and scaled to width a_j. Since the thickness of the sphere layer is not uniform we model the height of each particle as a random variable denoted z_j. The parameterization is illustrated in Figure 2. The overall height field is given by

$$z(x) = \sum_j (\phi_{x_j,a_j} + z_j)\Pi_{x_j,a_j} \tag{1}$$

Where the multiplication by Π_{x_j,a_j} in Eq. (1) is included to emphasize that the j'th particle area is limited to the corresponding local window.

Sampling Process 1 *Sample i.i.d copies of a particle shape ϑ. Particle centers x_j are distributed uniformly over the surface area, particle sizes and heights are sampled independently from distributions p_a, p_z.*

As in [Levin et al. 2013], assuming $\Delta_d \gg \Delta_c$ it is enough to compute the expected reflectance.

Claim 1 *Consider a surface modulation function $\mathfrak{a}$ whose phase is the height field sampled according to Sampling Process 1. The expected reflectance is given by:*

$$R_E(\mathbf{h}) = E\left[\mathfrak{I}(2\mathbf{h_x}/\lambda)\right] \tag{2}$$

with

$$E\left[\mathfrak{I}(\omega_x)\right] \approx \tag{3}$$

$$(1-|\tau|^2)E_{p_a}\left[a^2 \cdot \left|\Phi\left(\frac{\omega_x}{a^{-1}}\right)\right|^2\right] + |\tau|^2 \varrho\Pi\left(\frac{\omega_x}{\Delta_c^{-1}}\right) \tag{4}$$

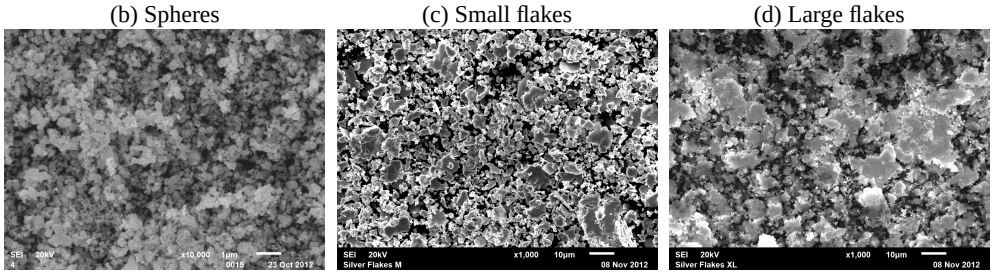

Figure 1: *A scanning electron microscope view of a photo-lithography surface and of three types of silver powders.*

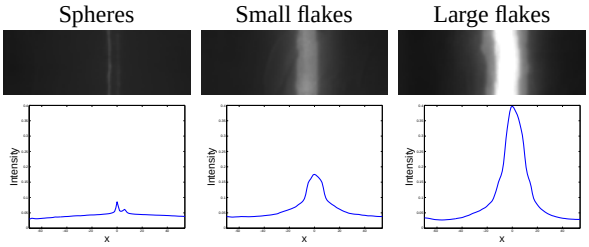

Figure 3: *Reflectance of silver powders. First row: An image of a cylindrical object covered with each type of powder, taken under white illumination (intensities cropped at 1). Second row: plot of the mean intensity in each column of the above.*

where $\Phi(\omega_x)$ denotes the Fourier transform of

$$\phi(x) = e^{-ik2\mathbf{h_z}\vartheta(x)}, \quad \tau = E_{p_z}[e^{-ik2\mathbf{h_z}z_j}] \tag{5}$$

and ϱ is a scaler defined in Appendix A.

We defer the proof to Appendix A. The result is very similar to the one derived in Claim 1 of [Levin et al. 2013], except that the sinc which represents in this claim the Fourier transform of the basic rect shape, is now replaced with Φ, the Fourier transform of a signal whose phase is the basic shape ϑ.

Applying this result to the case of spherical particles, Φ is the Fourier transform of a signal ϕ whose phase is a sphere. While this spectrum cannot be computed in closed form, a numerical calculation shows that it is almost flat. Intuitively, this result makes sense. Since the normals of a sphere are distributed equally in all orientations and hence, at least under a geometric optics model, it reflects light equally in all directions. The claim implies that the reflectance of a surface composed of spherical particles is a linear combination of a diffuse reflectance with a mirror reflectance. No other lobe type can be produced. This result is in agreement with the observations of [Johnson et al. 2011].

Note, that spheres lead to diffuse reflectance, regardless of the sphere particle size. In contrast, flakes lead to a metallic lobe reflectance where the lobe width is inherently dependent on the flakes' width. Flakes whose size is on the order of the wavelength ($\sim 0.5\mu m$) will result in diffuse reflectance, as explained in the discussion of physical step sizes and their corresponding lobe widths in [Levin et al. 2013].

2 Reflectance Measurements

Figure 1 shows an electron microscope scan of two silver flake powders[1] with different sized particles (mean particle width of $\sim 3\mu m$ and $\sim 6\mu m$) as well as a spherical powder (mean particle diameter $\sim 0.5\mu m$). To measure the reflectance we brushed the powders manually over a VHB transparent tape, wrapped the tape around a cylinder and illuminated it using a distant source. The resulting images can be seen in the first row of Figure 3. The second row of that figure shows a plot of the mean intensity as a function of the horizontal image position. As predicted by our analysis in Sec. 1 wider silver flakes generate a more glossy appearance. The spherical particles lead to a diffuse appearance with a narrow mirror spike. We can observe an additional shifted spike in the spheres cylinder image, since some of the light is transmitted into the tape layer and refracted back.

Metallic powders and the GelSight sensor: Figure 4 provides an additional comparison of these powder-based reflectances in the context of the elastomeric GelSight[2] sensor of Johnson et al. [2011]. This sensor is a slab of clear elastomer coated a with a metallic powder skin. When an object is pressed into the sensor, the reflective skin conforms to the shape of the object surface. Viewed through the elastomer, the surface appears to be painted by the reflective skin. This property allows for photometric stereo algorithms to be used to estimate the shape of the surface.

Johnson et al. [2011] invested much effort in searching for a powder with desirable properties. In the absence of a theory for predicting the reflectance properties of different particles, it was not clear how to find the best one. Commercial metallic paints which were explored in [Johnson and Adelson 2009] are composed of relatively large particles, limiting resolution. In the second generation of their sensor Johnson et al. [2011] used a spherical powder which produces a diffuse reflectance. As explained by the authors, matte reflectance is disadvantageous because it yields a low-contrast shading image that translates to a lower signal-to-noise ratio (SNR) when inferring surface normals and surface shape via photometric stereo. They mitigate this effect using grazing-angle illumination, which substantially complicates the required reconstruction algorithm because of induced shadows and uneven lighting.

Our analysis explains these effects, and it provides intuition that may enable future improvements in the shape resolution that can be achieved by elastomeric sensing. The analysis of Sec. 1 shows that the diffuse reflectance observed by Johnson et al. [2011] is caused by the spherical shape of the particles, and that this cannot be overcome without changing the particle shape. The same analysis shows that metallic flakes produce glossy reflectance that increases shading contrast. This suggests that flake-like shapes might make better

[1] Product of Ames Goldsmith
[2] http://www.gelsight.com/

coatings by enabling more robust reconstruction via direct lighting without shadows, and an increase in angular SNR.

To demonstrate this, Figure 4 compares our three metallic powders in an elastomeric sensing configuration. Under direct illumination the diffuse reflectance of the spherical powder produce low-contrast images, and surface detail can only be discerned when the light is moved to a grazing direction. In contrast, the flake-based powders produce glossy reflectance and high-contrast images, even when the lighting is near-frontal.

A Proof of reflectance properties

We now move to prove claim 1, which is a rather immediate generalization of claim 1 of [Levin et al. 2013], obtained when replacing the sinc with Φ, the Fourier transform of a general particle shape.

Claim 3 *Consider a surface modulation function* $\mathfrak{a}$ *whose phase is the height field sampled according to Sampling Process 1. The expected reflectance is given by*

$$R_E(\mathbf{h}) = E\left[\mathfrak{I}(2\mathbf{h_x}/\lambda)\right] \tag{6}$$

with

$$E\left[\mathfrak{I}(\omega_x)\right] \approx \tag{7}$$

$$(1-|\tau|^2)E_{p_a}\left[a^2\cdot\left|\Phi\left(\frac{\omega_x}{a^{-1}}\right)\right|^2\right] + |\tau|^2\varrho\Pi\left(\frac{\omega_x}{\Delta_c^{-1}}\right) \tag{8}$$

where $\Phi(\omega_x)$ *denotes the Fourier transform of*

$$\phi(x) = e^{-ik2\mathbf{h_z}\vartheta(x)}. \tag{9}$$

$$\tau = E_{p_z}[e^{-ik2\mathbf{h_z}z_j}] \tag{10}$$

$$\varsigma = E_{p_a}\left[\int_{-a/2}^{a/2}\phi(x/a)dx\right] \tag{11}$$

and $\varrho = \varsigma^2\Delta_c E_{p_a}[a]$

Proof of claim 3: To compute $E[\mathfrak{I}(\omega_x)]$ we first compute the expectation of the unblurred power spectrum $E[|\mathfrak{A}(\omega_x)|^2]$, and then, by the linearity of the expectation:

$$E[\mathfrak{I}(\omega_x)] = E[|\mathfrak{A}(\omega_x)|^2]\otimes\Pi_{0,\Delta_a/\lambda}. \tag{12}$$

That is, $E[\mathfrak{I}(\omega_x)]$ is obtained by blurring $E[|\mathfrak{A}(\omega_x)|^2]$.

We compute the expectation in two steps, first we think of step centers and widths x_j, a_j as observed values and compute the expected spectrum over all possible depth assignments z_j sampled independently from p_z. In the second step we compute expectations with respect to x_j, a_j.

Let n denote the number of steps averaged inside a dot

$$n = \frac{\Delta_d}{E_{p_a}[a]} \tag{13}$$

We define a set of random variables associated with the surface modulation function at each of the particles:

$$\psi_j = e^{-ik2\mathbf{h_z}(z_j+\phi_{x_j,a_j})}\Pi_{x_j,a_j}. \tag{14}$$

In the above notation we multiply the phase signal with the rect function Π_{x_j,a_j} to emphasis the fact that this random variable is zero outsize a segment of width a_j centered at x_j. The random variable ψ_j is a scaled and shifted version of the basic unit modulation function ϕ defined in Eq. (9) and we can write:

$$\psi_j(x) = e^{-ik2\mathbf{h_z}z_j}\phi\left(\frac{x-x_j}{a_j}\right) \tag{15}$$

We denote the Fourier transforms of the random variables ψ_j by Ψ_j, and in a similar way, they can be related to the basic unit Φ via scaling and phase shift:

$$\Psi_j(\omega_x) = e^{-2\pi i(x_j\omega_x+\frac{2\mathbf{h_z}z_j}{\lambda})}a_j\Phi\left(\frac{\omega_x}{a_j^{-1}}\right) \tag{16}$$

We can express the surface modulation function and its Fourier transform as a sum of the random variables representing each component Ψ_j. Thus,

$$\mathfrak{a} = \sum_{j=1}^{n}\psi_j \qquad \mathfrak{A} = \sum_{j=1}^{n}\Psi_j. \tag{17}$$

We can express the expected power spectrum as a sum of two terms, variance and squared mean. Using the fact that for a fixed sample of x_j, a_j, Ψ_j are independent random variables we get:

$$E_{p_z}[|\mathfrak{A}|^2] = \sum_{j=1}^{n}E_{p_z}\left[|\Psi_j - E_{p_z}[\Psi_j]|^2\right] + \left|\sum_{j=1}^{n}E_{p_z}[\Psi_j]\right|^2 \tag{18}$$

The variance term (first term in Eq. (18)) gives rise to the $|\Phi|^2$ part of the reflectance, the first term of Eq. (8), while the squared mean term (second term in Eq. (18)) leads to the impulse part of the reflectance, the second term of Eq. (8).

We start by computing the variance term. Taking expectations with respect to p_z we note

$$E_{p_z}[\Psi_j] = \tau e^{-2\pi i(x_j\omega_x)}a_j\Phi(\omega_x a_j) \tag{19}$$

Thus

$$E_{p_z}\left[|\Psi_j - E_{p_z}[\Psi_j]|^2\right] = E_{p_z}\left[\left|e^{-ik2\mathbf{h_z}z_j}-\tau\right|^2\right]a_j^2\left|\Phi(\omega_x a_j)\right|^2 \tag{20}$$

Using $\left|e^{-ik2\mathbf{h_z}z_j}\right|^2 = 1$ and $E_{p_z}\left[e^{-ik2\mathbf{h_z}z_j}\right] = \tau$ we get:

$$E_{p_z}\left[\left|e^{-ik2\mathbf{h_z}z_j}-\tau\right|^2\right] = (1-|\tau|^2) \tag{21}$$

hence

$$E_{p_z}\left[|\Psi_j - E_{p_z}[\Psi_j]|^2\right] = (1-|\tau|^2)a_j^2\left|\Phi(\omega_x a_j)\right|^2 \tag{22}$$

The expression in Eq. (22) does no longer depend on the centers x_j. After taking the expectation with respect to a_j we see that the variance term is indeed equal to the first term in Equation Eq. (8):

$$\sum_{j=1}^{n}E\left[|\Psi_j - E[\Psi_j]|^2\right] = n(1-|\tau|^2)E_{p_a}\left[a^2\cdot\left|\Phi\left(\frac{\omega_x}{a^{-1}}\right)\right|^2\right] \tag{23}$$

We now compute the second part of Eq. (18), the squared mean.

Due to the linearity of the Fourier transform $\sum_{j=1}^{n}E[\Psi_j]$ is the Fourier transform of $\sum_{j=1}^{n}E[\psi_j] = E[\sum_{j=1}^{n}\psi_j]$.

Since the sampling process is shift invariant we have an equal probability to see any part of a random variable at any x location. Thus $E_{p_z,p_a}[\sum_{j=1}^{n}\psi_j(x)]$ is a flat signal which does not depend on the location x. It is easy to see that:

$$E_{p_z,p_a}\left[\sum_{j=1}^{n}\psi_j(x)\right]=E_{p_z}\left[\sum_{j=1}^{n}e^{ik\mathbf{h_z}z_j}\right]E_{p_a}\left[\sum_{j=1}^{n}\phi(x/a)\right]=\tau\varsigma \tag{24}$$

Thus, the Fourier transform of the mean over a spatial support Δ_d is a narrow sinc around the zero frequency:

$$\sum_{j=1}^{n}E[\Psi_j]=\tau\varsigma\Delta_d\mathrm{sinc}\left(\frac{\omega_x}{\Delta_d^{-1}}\right) \tag{25}$$

Substituting Eqs. (25) and (23) in Eq. (18) yields

$$E\left[|\mathfrak{A}(\omega_x)|^2\right]\approx \tag{26}$$

$$n(1-|\tau|^2)E_{p_a}\left[a^2\cdot\mathrm{sinc}^2\left(\frac{\omega_x}{a^{-1}}\right)\right]+|\tau\varsigma|^2\Delta_d^2\mathrm{sinc}^2\left(\frac{\omega_x}{\Delta_d^{-1}}\right) \tag{27}$$

To conclude the proof, we need to compute $E[\mathfrak{I}(\omega_x)]$ from $E\left[|\mathfrak{A}(\omega_x)|^2\right]$. We follow Eq. (12) and blur $E\left[|\mathfrak{A}(\omega_x)|^2\right]$ with a rect of width $\Delta_c^{-1}=\Delta_a/\lambda$. The first term of Eq. (27) is relatively smooth and we assume it does not change that much by blurring, that is:

$$n(1-|\tau|^2)E_{p_a}\left[a^2\cdot\left|\Phi\left(\frac{\omega_x}{a^{-1}}\right)\right|^2\right]\otimes\Pi_{0,\Delta_c^{-1}}\approx$$

$$n(1-|\tau|^2)E_{p_a}\left[a^2\cdot\left|\Phi\left(\frac{\omega_x}{a^{-1}}\right)\right|^2\right] \tag{28}$$

The second term of Eq. (27) is a very narrow sinc of width Δ_d^{-1}. Assuming that $\Delta_d\gg\Delta_c$, then $\Delta_c^{-1}\gg\Delta_d^{-1}$. Hence, convolving the narrow sinc with the wider rect of width Δ_c^{-1} results roughly in a rect of width Δ_c^{-1}

$$\mathrm{sinc}^2\left(\frac{\omega_x}{\Delta_d^{-1}}\right)\otimes\Pi_{0,\Delta_c^{-1}}\approx\frac{\Delta_d^{-1}}{\Delta_c^{-1}}\Pi_{0,\Delta_c^{-1}}. \tag{29}$$

We further use $\Delta_d=nE_{p_a}[a]$ (Eq. (13)) and get

$$|\tau|^2\Delta_d^2\mathrm{sinc}^2\left(\frac{\omega_x}{\Delta_d^{-1}}\right)\otimes\Pi_{0,\Delta_c^{-1}}\approx n|\tau\varsigma|^2\Delta_cE_{p_a}[a]\Pi_{0,\Delta_c^{-1}} \tag{30}$$

Combining Eqs. (28) and (30) yields the desired result (Eq. (8)) up to a global scaling factor:

$$E[\mathfrak{I}(\omega_x)]\approx \tag{31}$$

$$n(1-|\tau|^2)E_{p_a}\left[a^2\cdot\left|\Phi\left(\frac{\omega_x}{a^{-1}}\right)\right|^2\right]+n|\tau|^2\varrho\Pi\left(\frac{\omega_x}{\Delta_c^{-1}}\right) \tag{32}$$

□

References

JOHNSON, M. K., AND ADELSON, E. H. 2009. Retrographic sensing for the measurement of surface texture and shape. In *Computer Vision and Pattern Recognition (CVPR)*, 1070–1077.

JOHNSON, M. K., COLE, F., RAJ, A., AND ADELSON, E. H. 2011. Microgeometry capture using an elastomeric sensor. *ACM Transactions on Graphics (Proc. ACM SIGGRAPH) 30*, 4, 46:1–46:8.

LEVIN, A., GLASNER, D., XIONG, Y., DURAND, F., FREEMAN, W., MATUSIK, W., AND ZICKLER, T. 2013. Fabricating brdfs at high spatial resolution using wave optics. *SIGGRAPH*.

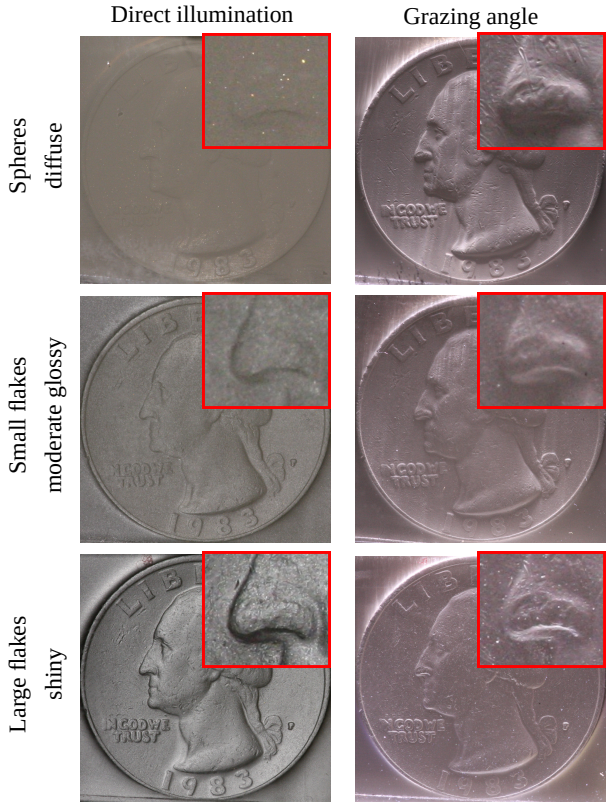

Figure 4: *Images of a U.S. quarter via a transparent elastomer pressed into different types of powders. The left column shows images taken with direct illumination. The images in the right column were taken with grazing angle illumination. Spherical powders have a diffuse reflectance and lack contrast under direct illumination, surface details are seen only when grazing illumination is used. Flake powders have a metallic reflectance and reveal much more information about surface orientation.*